2023 62nd IEEE Conference on Decision and Control (CDC)
December 13-15, 2023. Marina Bay Sands, Singapore

Investigation of Sub-synchronous Oscillation in HVDC-connected PMSG-based Offshore Wind Farm: Comprehensive Modeling and Analysis

Zhihao Zhang, Peng Kou, Mingyang Mei, Runze Tian, Yuanhang Zhang, and Deliang Liang

***Abstract*— This paper investigates the sub-synchronous oscillation occurring in high voltage direct current (HVDC)-connected permanent magnet synchronous generator (PMSG)-based offshore wind farm. To do so, firstly, a comprehensive system model is developed, which incorporates the dynamics of the PMSG-based wind energy conversion system (WECS), the ac collection grid, and the HVDC transmission system. Subsequently, small signal model of the comprehensive system is derived. Based on the small signal model, the critical system mode is obtained using modal analysis. Special attention is paid to the influence of sub-synchronous mode on the onshore grid. Moreover, the influence of controller parameters on the sub-synchronous mode is investigated, which facilitates the design of converter controllers in HVDC-integrated PMSG-based offshore wind farm. Additionally, the modal analysis results are verified through time-domain simulations.**

I. INTRODUCTION

The continuous and swift expansion of offshore wind energy provides a new avenue for addressing the dual pressures of energy requirement and environmental preservation [1]. Recent advances in wind power integration technology, specifically the utilization of permanent magnet synchronous generator (PMSG)-based wind energy conversion systems (WECSs) and high voltage direct current (HVDC) transmission systems, have enabled the large-scale exploitation of deep-sea wind energy [2]. Therefore, HVDC-connected PMSG-based offshore wind farm which incorporates the PMSG-based wind energy conversion system (WECS), the ac collection grid, and the HVDC transmission system, as shown in Fig.1, is a trend for offshore wind energy applications. Nevertheless, the interaction between PMSG-based offshore WECSs, ac collection grid and HVDC transmission system tends to cause severe sub-synchronous oscillation issues, thus threatening the stable operation of the onshore grid [3], [4]. As a result, there is an urgent need to investigate the sub-synchronous oscillation occurring in HVDC-connected PMSG-based offshore wind farm.

In early investigations of sub-synchronous oscillation, the literature mainly focused on the doubly-fed induction generator (DFIG)-based WECSs, which have been widely employed in onshore wind farms and early offshore wind farms [5], [6]. In recent years, some researchers have shifted their emphasis to sub-synchronous oscillation associated with PMSG-based WECSs [7], [8]. Although these studies satisfactorily revealed the mechanism of sub-synchronous oscillation associated with PMSG-based WECSs, they shared a common limitation, i.e., most of them only focused on the sub-synchronous oscillation occurring within the wind farm thus neglecting the possibility of such oscillations being transmitted to the utility grid through the HVDC transmission system. Specifically, most of them only investigated the sub-synchronous oscillation without considering the HVDC link and onshore HVDC station dynamics, i.e., only the left portion of the purple dashed line in Figure 1 was considered. Therefore, it remains uncertain whether the sub-synchronous oscillation occurring in offshore wind farm can exert an impact on the onshore grid thorough the long HVDC transmission cables.

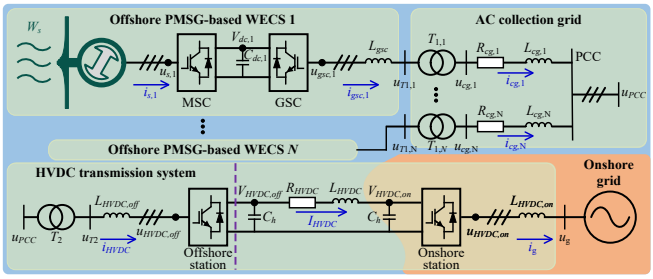

Fig. 1. Block diagram of the investigated system, which is composed of PMSG-based WECSs, ac collection grid, and HVDC transmission system.

Two methods, i.e., impedance analysis [9] and modal analysis [10], are commonly utilized to investigate the sub-synchronous oscillation associated with wind power integration systems. Impedance analysis is characterized by the idea of modularization. With this method, different parts of the system are modeled as separate modules and assembled together on various ports [11]. Although impedance analysis is an easy method to analyze interactive oscillation, it remains challenging to present the detailed influence of elements inside each module on the oscillation modes. For instance, impedance analysis cannot present the detailed influence of controller parameters on the sub-synchronous oscillation mode. In contrast, modal analysis can address this issue. With a more comprehensive and detailed system model, participation factors that indicate the influence of elements on the oscillation modes can be calculated.

Inspired by the above observations, in this paper, we presents an comprehensive investigation of sub-synchronous

This work was supported by the National Natural Science Foundation of China under Grant 52077165. (*Corresponding author: Peng Kou*)

All authors are with the State Key Laboratory of Electrical Insulation and Power Equipment, School of Electrical Engineering, Xian Jiaotong University, Xian 710049, China. (*e-mail: lyfxzzh@stu.xjtu.edu.cn, koupeng@mail.xjtu.edu.cn, meimingyang@stu.xjtu.edu.cn, zhangyh1998@stu.xjtu.edu.cn, dlliang@mail.xjtu.edu.cn*)

oscillation occurring in HVDC-connected PMSG-based offshore wind farm. To do so, firstly, in Section II, a comprehensive system model is developed, which incorporates the dynamics of the PMSG-based wind energy conversion system (WECS), the ac collection grid, and the HVDC transmission system. Subsequently, in Section III, small signal model of the comprehensive system is derived and modal analysis is introduced. Based on the small signal model, the critical system mode is obtained using modal analysis in Section IV. Special attention is paid to the influence of sub-synchronous mode on the onshore grid. Moreover, the influence of controller parameters on system mode is investigated, which facilitates the design of converter controllers in HVDC-integrated PMSG-based offshore wind farm. Additionally, the modal analysis results are verified through time-domain simulations.

II. COMPREHENSIVE MODEL OF HVDC-CONNECTED PMSG-BASED OFFSHORE WIND FARM

In this work, the investigated system is shown in Fig. 1, which is composed of PMSG-based WECSs, ac collection grid, HVDC transmission system and onshore grid. In this section, its comprehensive model will be developed.

A. Modeling of offshore PMSG-based WECS

As shown in Fig.1, offshore PMSG-based WECS comprises the blade, PMSG, and back-to-back converter. The back-to-back converter is composed of machine side converter (MSC), dc-link and grid side converter (GSC).

For offshore PMSG-based WECS, its overall model comprises the mechanical dynamic model and the electrical dynamic model. For each i-th offshore WECS, its mechanical dynamic can be described as

$$J_c \frac{\mathrm{d}\omega_i}{\mathrm{d}t} = \frac{P_{m,i} - P_{e,i}}{\omega_i} \tag{1}$$

where J_c is the combined inertia of wind blade and PMSG, $P_{m,i}$ is the mechanical power captured by the blade, whose dynamics can be found in [12], $P_{e,i}$ is the electrical power of PMSG, ω_i is the rotor mechanical angular speed of PMSG.

The overall electrical dynamic model of the i-th offshore WECS is composed of the *electrical models of PMSG* i, *MSC* i, *dc-link* i, and *GSC* i, which are typically formulated in the dq reference frame.

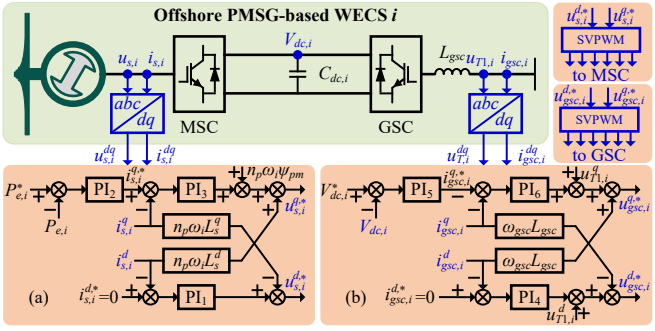

Fig. 2. Block diagram of the PMSG-based WECS, together with its controllers, (a) MSC controller, (b) GSC controller.

- *Electrical model of PMSG*: When the direction of q-axis is aligned with the voltage vector $u_{s,i}$, the electrical model of PMSG i is

$$\begin{aligned} u_{s,i}^d &= R_s i_{s,i}^d + L_s^d \frac{\mathrm{d}i_{s,i}^d}{\mathrm{d}t} - L_s^q n_p \omega_i i_{s,i}^q \\ u_{s,i}^q &= R_s i_{s,i}^q + L_s^q \frac{\mathrm{d}i_{s,i}^q}{\mathrm{d}t} + L_s^d n_p \omega_i i_{s,i}^d + n_p \omega_i \psi_{pm} \\ P_{e,i} &= 1.5 n_p \omega_i \psi_{pm} i_{s,i}^q \end{aligned} \tag{2}$$

Here, $i_{s,i}^d$ and $i_{s,i}^q$ are the output stator current of the i-th PMSG in dq-axis, $u_{s,i}^d$ and $u_{s,i}^q$ are the output stator voltage, R_s is the stator winding resistance, L_s^d and L_s^q are the dq-axis inductances, ψ_{pm} is the permanent magnetic flux, n_p is the number of pole pairs.

- *Electrical model of MSC*: For the offshore WECS, the transient dynamics of the MSC are much fast than electromagnetic and mechanical dynamics of the PMSG. In view of this, the dynamics of the MSC can be neglected [13]. That is, $u_{s,i}^d = u_{s,i}^{d,*}$ and $u_{s,i}^q = u_{s,i}^{q,*}$. Here, X^* represents the reference value of X. In practice, the reference values $u_{s,i}^{d,*}$ and $u_{s,i}^{q,*}$ are obtained from PI controllers of MSC, as shown in Fig.2 (a). From this figure, the dynamics of the MSC controller can be obtained, as follows

$$\begin{aligned} \frac{\mathrm{d}\varphi_{1,i}}{\mathrm{d}t} &= 0 - i_{s,i}^d \\ u_{s,i}^{d,*} &= K_{P1,i}(0 - i_{s,i}^d) + K_{I1,i}\varphi_{1,i} - L_s^q n_p \omega_i i_{s,i}^q \\ \frac{\mathrm{d}\varphi_{2,i}}{\mathrm{d}t} &= P_{e,i}^* - P_{e,i} \\ i_{s,i}^{q,*} &= K_{P2,i}(P_{e,i}^* - P_{e,i}) + K_{I2,i}\varphi_{2,i} \\ \frac{\mathrm{d}\varphi_{3,i}}{\mathrm{d}t} &= i_{s,i}^{q,*} - i_{s,i}^q \\ u_{s,i}^{q,*} &= K_{P3,i}(i_{s,i}^{q,*} - i_{s,i}^q) + K_{I3,i}\varphi_{3,i} \\ &\quad + L_s^d n_p \omega_i i_{s,i}^d + n_p \omega_i \psi_{pm} \end{aligned} \tag{3}$$

Here, $\varphi_{1,i}$, $\varphi_{2,i}$ and $\varphi_{3,i}$ are introduced intermediate variables, $K_{P1,i}$ and $K_{I1,i}$ are the d-axis inner loop controller parameters, $K_{P2,i}$ and $K_{I2,i}$ are the q-axis outer loop controller parameters, $K_{P3,i}$ and $K_{I3,i}$ are the q-axis inner loop controller parameters.

- *Electrical model of dc-link*: The resistance of the dc-link can be omitted due to its short length. As a result, the dynamics of the dc-link is mainly characterized by the filter capacitor $C_{dc,i}$. Assuming the converters loss is negligible, the dynamics of the dc-link can be represented by

$$C_{dc,i} V_{dc,i} \frac{\mathrm{d}V_{dc,i}}{\mathrm{d}t} = P_{e,i} - P_{gsc,i} \tag{4}$$

where $V_{dc,i}$ is the dc-link voltage, $P_{gsc,i}$ is the output power of the GSC.

- *Electrical model of GSC*: At the grid side of the GSC, an inductor L_{gsc} is typically employed to filter out the high-order harmonics in output current. When the direction of q-axis is aligned with the voltage vector $u_{T1,i}$, the dynamics

of the inductor is

$$\begin{aligned} u^d_{gsc,i} &= L_{gsc}\frac{\mathrm{d}i^d_{gsc,i}}{\mathrm{d}t} - L_{gsc}\omega_{gsc}i^q_{gsc,i} + u^d_{T1,i} \\ u^q_{gsc,i} &= L_{gsc}\frac{\mathrm{d}i^q_{gsc,i}}{\mathrm{d}t} + L_{gsc}\omega_{gsc}i^d_{gsc,i} + u^q_{T1,i} \end{aligned} \tag{5}$$

where $i^d_{gsc,i}$ and $i^q_{gsc,i}$ are the GSC output current, $u^d_{gsc,i}$ and $u^q_{gsc,i}$ are the GSC output voltage at fundamental collection grid frequency ω_{gsc}, $u^d_{T1,i}$ and $u^q_{T1,i}$ are the voltage of the low-voltage side in transformer $T_{1,i}$. With these mathematical notations, the output power of the GSC $P_{gsc,i}$ in (4) can be calculated by

$$P_{gsc,i} = u^d_{gsc,i}i^d_{gsc,i} + u^q_{gsc,i}i^q_{gsc,i} \tag{6}$$

The transient of GSC, similar to that of MSC, can be considered negligible. Consequently, only the dynamics of the MSC controller is taken into account. Fig.2(b) illustrates the block diagram of the GSC controller, which is designed to achieve a zero reactive power of the GSC and maintain a constant voltage of the dc-link. From this figure, we can get the dynamics of the GSC controller, as follows

$$\begin{aligned} \frac{\mathrm{d}\varphi_{4,i}}{\mathrm{d}t} &= 0 - i^d_{gsc,i} \\ u^{d,*}_{gsc,i} &= K_{P4,i}(0 - i^d_{gsc,i}) + K_{I4,i}\varphi_{4,i} \\ &\quad - L_{gsc}\omega_{gsc}i^q_{gsc,i} + u^d_{t1,i} \\ \frac{\mathrm{d}\varphi_{5,i}}{\mathrm{d}t} &= V^*_{dc,i} - V_{dc,i} \\ i^{q,*}_{gsc,i} &= K_{P5,i}(V^*_{dc,i} - V_{dc,i}) + K_{I5,i}\varphi_{5,i} \\ \frac{\mathrm{d}\varphi_{6,i}}{\mathrm{d}t} &= i^{q,*}_{gsc,i} - i^q_{gsc,i} \\ u^{q,*}_{gsc,i} &= K_{P6,i}(i^{q,*}_{gsc,i} - i^q_{gsc,i}) + K_{I6,i}\varphi_{6,i} \\ &\quad + L_{gsc}\omega_{gsc}i^d_{gsc,i} + u^q_{t1,i} \end{aligned} \tag{7}$$

Here, $\varphi_{4,i}$, $\varphi_{5,i}$ and $\varphi_{6,i}$ are introduced intermediate variables, $K_{P4,i}$ and $K_{I4,i}$ are the d-axis inner loop controller parameters, $K_{P5,i}$ and $K_{I5,i}$ are the q-axis outer loop controller parameters, $K_{P6,i}$ and $K_{I6,i}$ are the q-axis inner loop controller parameters.

The mechanical dynamic model (1), together with the electrical dynamic model (2) $\sim$ (7), constitute the overall dynamic model of the i-th offshore WECS.

B. Modeling of ac collection grid

In the investigated offshore wind farm shown in Fig.1, an ac collection grid consisting of N feeders connects all WECSs, thereby transferring the power captured by wind turbines. Each WECS connects to the feeder via a step-up transformer $T_{1,i}$. Using such an arrangement, the low-voltage output of the WECS is stepped up to a medium-voltage level, resulting in decreased power loss during the power collection process.

The step-up transformer can be approximated as the ideal one after its impedance is converted into the medium-voltage feeder line. As a result, we have

$$u_{cg,i} = k_1 u_{T1,i}, \quad i_{cg,i} = i_{gsc,i}/k_1 \tag{8}$$

where k_1 represents the transformer ratio of $T_{1,i}$, $u_{cg,i}$ is the voltage of the high-voltage side in transformer $T_{1,i}$, $i_{cg,i}$ is the the current of the i-th feeder.

Moreover, the dynamics of the medium-voltage feeder line can be described as

$$\begin{aligned} u^d_{cg,i} &= R_{cg,i}i^d_{cg,i} + L_{cg,i}\frac{\mathrm{d}i^d_{cg,i}}{\mathrm{d}t} - L_{cg,i}\omega_{gsc}i^q_{cg,i} + u^d_{PCC} \\ u^q_{cg,i} &= R_{cg,i}i^q_{cg,i} + L_{cg,i}\frac{\mathrm{d}i^q_{cg,i}}{\mathrm{d}t} + L_{cg,i}\omega_{gsc}i^d_{cg,i} + u^q_{PCC} \end{aligned} \tag{9}$$

Here, $R_{cg,i}$ and $L_{cg,i}$ are the equivalent resistance and inductance of the i-th feeder, incorporating both the line parameters and the equivalent parameters of the transformer, u^d_{PCC} and u^q_{PCC} are the voltage of the point of common coupling (PCC).

C. Modeling of HVDC transmission system

The ac collection grid voltage u_{PCC} is stepped up to the high transmission voltage by the step-up transformer T_2, and then the power is delivered to the utility grid via the HVDC transmission system, as shown in Fig.3. In this subsection, the HVDC transmission system model is constructed, which is composed of three parts, i.e., offshore HVDC station, HVDC link and onshore HVDC station.

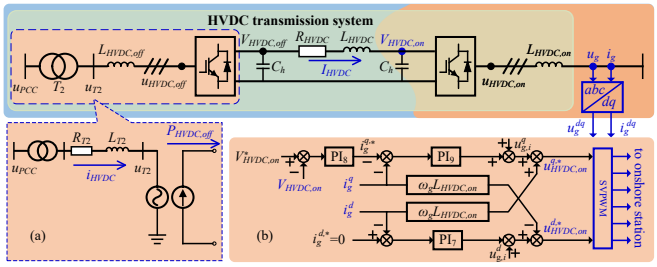

Fig. 3. Block diagram of the HVDC transmission system, together with (a) offshore HVDC station equivalent model, (b) onshore HVDC station controller.

- *Offshore HVDC station model*: After the impedance of T_2 is converted into the high-voltage side, the mathematical relationship between u_{PCC} and u_{T2} can be expressed as

$$\begin{aligned} k_2 u^d_{PCC} &= R_{T2}i^d_{HVDC} + L_{T2}\frac{\mathrm{d}i^d_{HVDC}}{\mathrm{d}t} \\ &\quad - L_{T2}\omega_{gsc}i^q_{HVDC} + u^d_{T2} \\ k_2 u^q_{PCC} &= R_{T2}i^q_{HVDC} + L_{T2}\frac{\mathrm{d}i^q_{HVDC}}{\mathrm{d}t} \\ &\quad + L_{T2}\omega_{gsc}i^d_{HVDC} + u^q_{T2} \\ i^d_{HVDC} &= \frac{1}{k_2}\sum_{i=1}^{N} i^d_{cg,i}, \; i^q_{HVDC} = \frac{1}{k_2}\sum_{i=1}^{N} i^q_{cg,i} \end{aligned} \tag{10}$$

Here, k_2 represents the transformer ratio of T_2, R_{T2} and L_{T2} are the transformer equivalent resistance and inductance converted into the high-voltage side, i^d_{HVDC} and i^q_{HVDC} are the input current of offshore HVDC station.

The offshore HVDC station is operated with a control system that regulates the amplitude and frequency of u_{T2} to remain constant. To reduce the complexity of the model, the offshore HVDC station can be represented by an ideal

voltage source on the ac side and a constant power source on the dc side, as shown in Fig.3(a). This simplified model assumes ideal voltage and current conversion characteristics for the offshore HVDC station and can effectively reflect its basic features and performance [14].

• *HVDC link model*: On the dc side of HVDC transmission system, two capacitors C_h are placed for dc-link filtering. Additionally, the HVDC cables can be characterized by an equivalent resistance and inductance. From these points of view, the dynamics of the HVDC link can be described as

$$\begin{aligned} P_{HVDC,off} &= C_h V_{HVDC,off}\frac{\mathrm{d}V_{HVDC,off}}{\mathrm{d}t} \\ &\quad + I_{HVDC}V_{HVDC,off} \\ V_{HVDC,off} &= R_{HVDC}I_{HVDC} + L_{HVDC}\frac{\mathrm{d}I_{HVDC}}{\mathrm{d}t} \\ P_{HVDC,on} &= -C_h V_{HVDC,on}\frac{\mathrm{d}V_{HVDC,on}}{\mathrm{d}t} \\ &\quad + I_{HVDC}V_{HVDC,on} \end{aligned} \tag{11}$$

Here, $P_{HVDC,off}$ is the output active power of offshore HVDC station and can be calculated using $P_{HVDC,off} = u^d_{T2}i^d_{HVDC} + u^q_{T2}i^q_{HVDC}$, $V_{HVDC,off}$ and $V_{HVDC,on}$ denote the voltage at the offshore and onshore HVDC stations, respectively, I_{HVDC} represents the direct current flowing through the transmission cables, R_{HVDC} and L_{HVDC} are the equivalent resistance and inductance of the transmission cables.

• *Onshore HVDC station model*: At the grid side of the onshore HVDC station, an inductor $L_{HVDC,on}$ is typically employed to filter out the high-order harmonics in output current. When the direction of q-axis is aligned with the onshore grid voltage vector u_g, the dynamics of the inductor is

$$\begin{aligned} u^d_{HVDC,on} &= L_{HVDC,on}\frac{\mathrm{d}i^d_g}{\mathrm{d}t} - L_{HVDC,on}\omega_g i^q_g + u^d_g \\ u^q_{HVDC,on} &= L_{HVDC,on}\frac{\mathrm{d}i^q_g}{\mathrm{d}t} + L_{HVDC,on}\omega_g i^d_g + u^q_g \end{aligned} \tag{12}$$

where i^d_g and i^q_g are the output current of the onshore HVDC station, $u^d_{HVDC,on}$ and $u^q_{HVDC,on}$ are the output voltage of the onshore HVDC station at fundamental grid frequency ω_g, u^d_g and u^q_g are the grid voltage, which is assumed as an ideal voltage source. With these mathematical notations, the output power of the onshore HVDC station $P_{HVDC,on}$ in (11) can be calculated by

$$P_{HVDC,on} = u^d_g i^d_g + u^q_g i^q_g \tag{13}$$

The transient of onshore HVDC station is assumed to be negligible, similar to that of MSC and GSC. Therefore, only the onshore HVDC station controller dynamics is considered. Fig.3(b) depicts the block diagram of this controller, which is designed to achieve a zero reactive power and maintain a constant voltage of the HVDC-link. From this figure, we can get the dynamics of the onshore HVDC controller, as follows

$$\begin{aligned} \frac{\mathrm{d}\varphi_7}{\mathrm{d}t} &= 0 - i^d_g \\ u^{d,*}_{HVDC,on} &= K_{P7}(0 - i^d_g) + K_{I7}\varphi_7 \\ &\quad - L_{HVDC,on}\omega_g i^q_g + u^d_g \\ \frac{\mathrm{d}\varphi_8}{\mathrm{d}t} &= v^*_{HVDC,on} - v_{HVDC,on} \\ i^{q,*}_g &= K_{P8}(v^*_{HVDC,on} - v_{HVDC,on}) + K_{I8}\varphi_8 \\ \frac{\mathrm{d}\varphi_9}{\mathrm{d}t} &= i^{q,*}_g - i^q_g \\ u^{q,*}_{HVDC,on} &= K_{P9}(i^{q,*}_g - i^q_g) + K_{I9}\varphi_9 \\ &\quad + L_{HVDC,on}\omega_g i^d_g + u^q_g \end{aligned} \tag{14}$$

Here, φ_7, φ_8 and φ_9 are introduced intermediate variables, K_{P7} and K_{I7} are the d-axis inner loop controller parameters, K_{P8} and K_{I8} are the q-axis outer loop controller parameters, K_{P9} and K_{I9} are the q-axis inner loop controller parameters.

III. MODAL ANALYSIS OF HVDC-CONNECTED PMSG-BASED OFFSHORE WIND FARM

Upon completion of the HVDC-connected PMSG-based offshore wind farm model, it is evident that the system exhibits strong coupled and nonlinear characteristics, thereby posing a significant challenge for stability analysis. To fill this gap, in this section, small signal model is derived based on the comprehensive model constructed in Section II. With the small signal model, we can evaluate the capability of the power system to recover an acceptable state of equilibrium when subjected to small disturbances using modal analysis.

A. Small Signal Model of HVDC-connected PMSG-based Offshore Wind Farm

The comprehensive model constructed in Section II can be written in the vector-matrix notation, as follows

$$\frac{\mathrm{d}\mathbf{x}}{\mathrm{d}t} = \mathbf{f}(\mathbf{x},\ \mathbf{u}) \tag{15}$$

where $\mathbf{x}$ is the state vector, $\mathbf{u}$ is the control vector.

In this work, the offshore wind turbines are assumed operating at the same condition. In other words, the variables of all offshore WECSs are identical, meaning that $[\omega_{m,i},\ i^d_{s,i},\ i^q_{s,i},\ \varphi_{1,i},\ \varphi_{2,i},\ \varphi_{3,i},\ V_{dc,i},\ \varphi_{4,i},\ \varphi_{5,i},\ \varphi_{6,i}]^{\mathrm{T}}$ are equal to $[\omega_m,\ i^d_s,\ i^q_s,\ \varphi_1,\ \varphi_2,\ \varphi_3,\ V_{dc},\ \varphi_4,\ \varphi_5,\ \varphi_6]^{\mathrm{T}}$.

With these notations, the state vector and control vector of the investigated system are given as $\mathbf{x} = [\omega_m,\ i^d_s,\ i^q_s,\ \varphi_1,\ \varphi_2,\ \varphi_3,\ V_{dc},\ \varphi_4,\ \varphi_5,\ \varphi_6,\ i^d_{HVDC},\ i^q_{HVDC},\ V_{HVDC,off},\ I_{HVDC},\ V_{HVDC,on},\ \varphi_7,\ \varphi_8,\ \varphi_9,\ i^d_g,\ i^q_g]^{\mathrm{T}}$ and $\mathbf{u} = [P^*_e,\ V^*_{dc},\ V^*_{HVDC,on}]^{\mathrm{T}}$, where P^*_e is the active power reference of all offshore wind turbines.

By applying Taylor series expansion and omitting the terms involving second and higher order powers of $\Delta\mathbf{x}$ and $\Delta\mathbf{u}$, the first-order approximation of the investigated system, i.e., small signal model, can be obtained, as follows

$$\frac{\mathrm{d}\Delta\mathbf{x}}{\mathrm{d}t} = \mathbf{A}\Delta\mathbf{x} + \mathbf{B}\Delta\mathbf{u} \tag{16}$$

Here, $\mathbf{A}$ is the state matrix, $\mathbf{B}$ is the control matrix. Please refer to [15] for more details about the derivation of the small signal model.

B. Modal Analysis with Small Signal Model

Based on the linearized small signal model, the stability of the investigated system can be studied using the modal analysis. To facilitate the modal analysis, three major elements should be calculated, i.e., eigenvalue, mode shape and participation factor.

- *Eigenvalue*: The eigenvalues of the state matrix $\mathbf{A}$ correspond to the system modes. In this work, with $n_s = 20$ state variables, the matrix $\mathbf{A}$ has $n_s = 20$ eigenvalues, indicating the presence of $n_s = 20$ modes in the investigated system. For the k-th eigenvalue $\lambda_k = \sigma_k + j\omega_k$, its imaginary component ω_k represents the frequency of the k-the system mode, while the real component σ_k corresponds to the damping. That is

$$f_k = \omega_k/(2\pi),\ \zeta_k = -\sigma_k/\sqrt{{\sigma_k}^2 + {\omega_k}^2} \tag{17}$$

Here, f_k and ζ_k are the frequency and damping ratio of the k-th mode.

The eigenvalues of the the matrix $\mathbf{A}$ can be calculated by

$$\det(\mathbf{A} - \lambda\mathbf{I}) = 0 \tag{18}$$

where $\mathbf{I}$ is the $n_s \times n_s$ identity matrix.

Moreover, the right eigenvector Φ_k and left eigenvector Ψ_k of λ_k can also be derived, as follows

$$\begin{aligned} (\mathbf{A} - \lambda_k\mathbf{I})\Phi_k &= 0 \\ \Psi_k(\mathbf{A} - \lambda_k\mathbf{I}) &= 0 \\ \Psi_k\Phi_k &= 1 \end{aligned} \tag{19}$$

Here, Φ_k is the $n_s \times 1$ column vector, Ψ_k is the $1 \times n_s$ row vector.

- *Mode shape*: The mode shape is given by the right eigenvector Φ_k and describes the relative activity of the state variables when a particular mode is excited. Specifically, the degree of activity of the l-th state variable $\mathbf{x}_l$ in the k-th mode is determined by the l-th element of the vector Φ_k [15]. If the magnitude of the l-th element of vector Φ_k is significant, then the corresponding eigenvalue λ_k is one of the dominant modes influencing the l-th state variable of the system.
- *Participation factor*: Opposed to the mode shape, the participation factor p_{lk} is a measure of the relative participation of the l-th state variable in the k-th mode. The participation factor can be computed using the following formula

$$p_{lk} = \Phi_{lk}\Psi_{kl} \tag{20}$$

where Φ_{lk} is the l-th element of the right eigenvector Φ_k, Ψ_{kl} is the l-th element of the left eigenvector Ψ_k.

By utilizing the eigenvalues, it is feasible to determine the critical system modes. Further, the degree of activity of the state variables in these critical system modes can be revealed with the mode shapes. Additionally, through the participation factors, one can identify which state variables have significant effects on the system modes.

IV. Case Studies on Stability Enhancment of HVDC-Connected PMSG-Based Offshore Wind Farm

In this section, several sets of case studies are employed to investigate the stability of the HVDC-connected PMSG-based offshore wind farm. All case studies are implemented in MATLAB and special attention is focused on the sub-synchronous oscillation. The investigated system structure diagram is shown in Fig.1 and the controllers diagrams are presented in Fig.2 and Fig.3. To achieve the balance between simulation speed and accuracy, all of the offshore WECS are assumed operating at the same condition. The parameters of the investigated system are listed in the Appendix.

A. Sub-synchronous mode in the investigated system

In this subsection, the stability of the HVDC-connected PMSG-based offshore wind farm is investigated using the modal analysis. Table AI and Table AII present the controllers parameters, which are roughly tuned by trial and error. The initial operating point of the investigated system is set to $P_{e,i} = 3\text{MW}$, $V_{dc,i} = 5.4\text{kV}$ and $V_{HVDC,n} = 100\text{kV}$. Moreover, all the offshore WECSs are assumed to face the same wind speeds, i.e., 11m/s.

The Eigenvalues of the investigated system are calculated and listed in Table I. Each eigenvalue corresponds to a mode. From Table I, we can see that there are four complex pair of eigenvalues, i.e., $\lambda_2\&\lambda_3$, $\lambda_4\&\lambda_5$, $\lambda_6\&\lambda_7$ and $\lambda_{10}\&\lambda_{11}$, which demonstrates that there are four oscillation modes in the investigated system at its initial operating point. Among all oscillation modes, the system mode corresponding to $\lambda_{10}\&\lambda_{11}$ is distinguished by the oscillation frequency of 23.36 Hz, a value that lies within the spectrum of sub-synchronous oscillations. In view of this, this mode can be identified as the sub-synchronous oscillation mode. The aforementioned mode is also characterized by the minimum damping ratio, i.e., 0.11, indicating that it may deteriorate the stable operation of the onshore grid.

TABLE I
EIGENVALUES OF THE INVESTIGATED SYSTEM AT INITIAL OPERATING POINT

Eigenvalues	Values	Frequency (Hz)	Damping ratio
λ_1	$-174.12 + j0$	0	1
$\lambda_2\&\lambda_3$	$-162.94 \pm j826.26$	131.50	0.19
$\lambda_4\&\lambda_5$	$-102.93 \pm j286.50$	45.60	0.34
$\lambda_6\&\lambda_7$	$-86.45 \pm j34.83$	5.54	0.93
λ_8	$-48.01 + j0$	0	1
λ_9	$-37.43 + j0$	0	1
$\lambda_{10}\&\lambda_{11}$	$-16.34 \pm j146.79$	23.36	0.11
λ_{12}	$-10.25 + j0$	0	1
λ_{13}	$-10.12 + j0$	0	1
λ_{14}	$-8.90 + j0$	0	1
λ_{15}	$-4.04 + j0$	0	1
$\lambda_{16} \sim \lambda_{20}$	$(-1.5 \sim 0) + j0$	0	1

Fig.4 presents the mode shape of the investigated system which elucidates the degree of influence of the k-th system mode on the l-th state variable. Fig.4(b) illustrates the mode shape of sub-synchronous oscillation, which is the critical

mode with respect to the system stability. Fig.4(b) reveals that the sub-synchronous oscillation indeed manifests itself in the offshore WECS (i.e., $\mathbf{x}_7 = V_{dc}$). Notably, such oscillation also occurs in the HVDC transmission system (i.e., $\mathbf{x}_{13} = V_{HVDC,off}$, $\mathbf{x}_{14} = I_{HVDC}$, and $\mathbf{x}_{15} = V_{HVDC,on}$) and onshore grid (i.e., $\mathbf{x}_{20} = i_g^q$). From this point of view, the sub-synchronous oscillation within offshore wind farm can exert an impact on the onshore grid thorough the long HVDC transmission cables. In other words, such oscillation has the potential to introduce disturbances into the onshore grid, thereby affecting its overall stability and reliability. Therefore, it is imperative to carefully monitor and mitigate these oscillations in order to ensure the smooth operation of the power system.

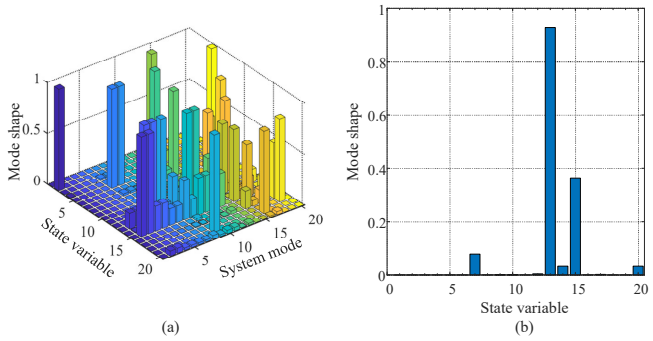

Fig. 4. Shape of (a) all system modes, (b) sub-synchronous mode.

To further verify the above findings, the time-domain simulation is facilitated. To do so, at $t = 2.0$s, the power reference P_e^* for each offshore WECS is increased from 3MW to 3.3MW. The dynamics in offshore HVDC station voltage and onshore HVDC station power are presented in Fig.5. From this figure, we can see that after the step increase of P_e^*, both the offshore HVDC station voltage $V_{HVDC,off}$ and onshore HVDC station power $P_{HVDC,on}$ are increased. Regrettably, in both the voltage and power dynamics of the HVDC system, exponential-decaying sinusoidal waveforms with a frequency of 23.64Hz are observed. These waveforms are indicative of sub-synchronous oscillation, which have been identified as a oscillation mode through the above modal analysis, as shown in Table I. This is an undesirable phenomenon that can adversely affect the performance of the system. As a result, it necessitates taking an appropriate measure to mitigate its effects and ensure the reliable operation of the system.

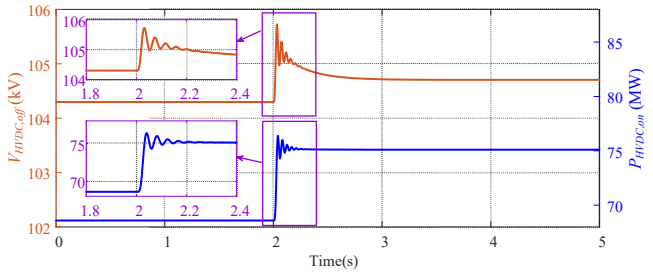

Fig. 5. Dynamics in offshore HVDC station voltage and onshore HVDC station power.

To obtain deeper insights into mitigating the sub-synchronous oscillation, it is crucial to ascertain which element dominates this particular oscillation mode. To accomplish this, in Fig.6, the participation factors are calculated and presented, which indicate the degree of influence of the l-th state variable on the k-th system mode. Considering the fact that the sub-synchronous oscillation is the critical mode, the participation factors of this particular mode are further illustrated in Fig.6(b). From this figure, it is evident that the sub-synchronous oscillation is most strongly influenced by the 7-th and 12-th state variables, i.e., $\mathbf{x}_7 = V_{dc}$ and $\mathbf{x}_{12} = i_{HVDC}^q$, as they exhibit the highest relative participation. Given that i_{HVDC}^q is dependent to ac side current of GSC i_{gsc}^q, and V_{dc} is the dc side voltage of GSC, the GSC in offshore wind farm plays a critical role in dominating the sub-synchronous oscillation. Subsequently, it is recommended to modify the parameters of the GSC controllers to mitigate this particular oscillation mode. This is going to be discussed in the next subsection.

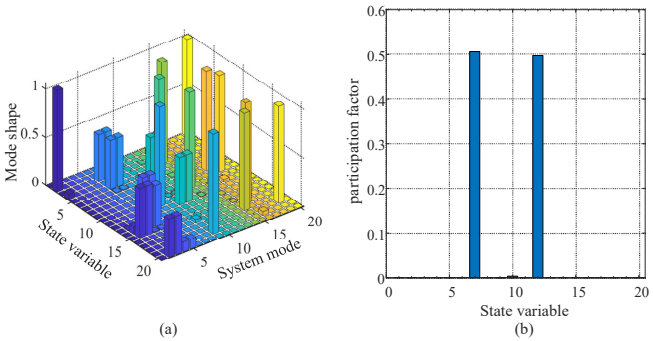

Fig. 6. Participation factor of (a) all system modes, (b) sub-synchronous mode.

B. Influence of GSC controller's parameters on sub-synchronous mode

In this subsection, the influence of the GSC controller's parameters on the sub-synchronous mode will be investigated. In fact, there are three PI-based controllers in GSC, i.e., d-axis inner loop controller, q-axis outer loop controller, and q-axis inner loop controller. Since the two inner loops are current loops which have already undergone open loop tuning and demonstrated satisfactory performance, only the influence of q-axis outer loop controller's parameters on sub-synchronous mode is investigated.

Fig.7 illustrates the eigenvalue loca corresponding to sub-synchronous mode with different GSC controller parameters $K_{P5,i}$ and $K_{I5,i}$. The blue line in this figure indicates that with the decreasing $K_{P5,i}$, both the real and imaginary components of the eigenvalue corresponding to the sub-synchronous mode decrease in magnitude, and the imaginary part decreases more significantly. This results in an increase in the damping ratio of the sub-synchronous mode, thereby enhancing the stability of the investigated system. Regrettably, we cannot continuously improve the system stability by decreasing $K_{P5,i}$. The reason lies in that when $K_{P5,i}$ is too small, i.e., $K_{P5,i} < 0.079$, some of the system's eigenvalues will move to the right-half plane, which means that the system will diverge and become unstable. Considering that the damping ratio of the sub-synchronous mode does not

change significantly when $K_{P5,i}$ is in the range of $0.08 \sim 0.1$, the modified $K_{P5,i}$ is chosen as 0.1.

Moreover, the orange line in Fig.7 reveals that as $K_{I5,i}$ decreases, the real component of the eigenvalue corresponding to the sub-synchronous mode increases in magnitude while the imaginary part remains almost constant. This also results in an increase in the damping ratio of the sub-synchronous mode, thereby enhancing the stability of the investigated system. Analogously, we cannot continuously improve the system stability by decreasing $K_{I5,i}$. When $K_{I5,i}$ is too small, i.e., $K_{P5,i} < 0.1$, the damping ratio of the sub-synchronous mode does not change significantly. From this point of view, the modified $K_{I5,i}$ is chosen as 0.1.

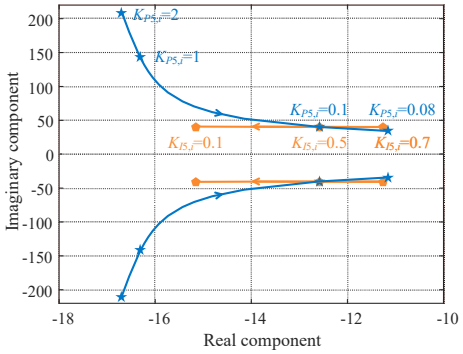

Fig. 7. Eigenvalue loca corresponding to sub-synchronous mode with different GSC controller parameters.

Table II lists the eigenvalues of the investigated system with the modified GSC controller parameters. From this table, we can find that with the modified GSC controller parameters, the frequency of the sub-synchronous oscillation mode decreases from 23.36Hz to 6.49Hz. Meanwhile, the damping ratio of this critical mode increases from 0.11 to 0.35, indicating an improvement in the stability of the investigated system.

TABLE II

EIGENVALUES OF THE INVESTIGATED SYSTEM AT MODIFIED OPERATING POINT

Eigenvalues	Values	Frequency (Hz)	Damping ratio
λ_1	$-174.12 + j0$	0	1
λ_2&λ_3	$-162.94 \pm j826.26$	131.50	0.19
λ_4&λ_5	$-102.93 \pm j286.50$	45.60	0.34
λ_6&λ_7	$-86.45 \pm j34.83$	5.54	0.93
λ_8	$-48.01 + j0$	0	1
λ_9	$-37.43 + j0$	0	1
λ_{10}&λ_{11}	$-15.15 \pm j40.80$	6.49	0.35
λ_{12}	$-10.25 + j0$	0	1
λ_{13}	$-11.65 + j0$	0	1
λ_{14}	$-8.90 + j0$	0	1
λ_{15}	$-4.04 + j0$	0	1
$\lambda_{16} \sim \lambda_{20}$	$(-1.5 \sim 0) + j0$	0	1

The above findings are also verified with the time-domain simulation. As the simulation setup in Section IV-A, the power reference P_e^* for each offshore WECS is increased from 3MW to 3.3MW at $t = 2.0$s. Fig.8 illustrates the dynamics in offshore HVDC station voltage and onshore HVDC station power with the modified GSC controller parameters. From this figure, it is evident that after the step increase of P_e^*, both the offshore HVDC station voltage $V_{HVDC,off}$ and onshore HVDC station power $P_{HVDC,on}$ are increased in a smoother way. This indicates that the sub-synchronous oscillation is significantly suppressed.

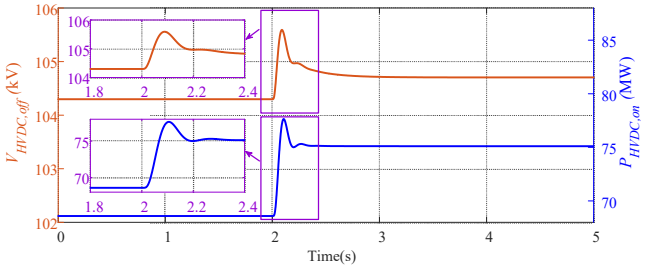

Fig. 8. Dynamics in offshore HVDC station voltage and onshore HVDC station power with the modified GSC controller parameters.

V. CONCLUSIONS

This paper investigates the sub-synchronous oscillation occurring in HVDC-connected PMSG-based offshore wind farm. The key contributions of this paper are threefold

- For the first time, the sub-synchronous oscillation is investigated with the modal analysis and the comprehensive model which incorporates the dynamics of the offshore PMSG-based WECSs, ac collection grid and HVDC transmission system.
- For the first time in the context of HVDC-connected PMSG-based deep-sea wind farm, with the mode shape technique, it is revealed that the sub-synchronous oscillation within offshore wind farm can exert an impact on the onshore grid thorough the long HVDC transmission cables.
- With the eigenvalue and the participation factor, the crucial controller parameters corresponding to the sub-synchronous oscillation are identified and modified, thus improving the stability of the investigated system.

APPENDIX

TABLE AI

PARAMETERS OF THE PMSG-BASED WECS

PMSG and back-to-back converter	
PMSG rated power (MVA)	5
Stator winding resistance R_s (mΩ)	72.2
d and q axis inductance L_s^d, L_s^q (mH)	2.6
Number of pole pairs n_p	145
permanent magnetic flux ψ_{pm} (Wb)	10.28
Combined inertia J_c (kgm^2)	1.06×10^7
Nominal value of the dc link $V_{dc,i}$ (kV)	5.4
Filter capacitor $C_{dc,i}$ (mF)	2
Filter inductor L_{gsc} (mH)	1
Number of the WECSs N	24
MSC controller	
d-axis inner loop controller $K_{P1,i}$, $K_{I1,i}$	0.4, 4
q-axis outer loop controller $K_{P2,i}$, $K_{I2,i}$	1×10^{-7}, 1.25×10^{-2}
q-axis inner loop controller $K_{P3,i}$, $K_{I3,i}$	0.4, 4
GSC controller	
d-axis inner loop controller $K_{P4,i}$, $K_{I4,i}$	5×10^{-2}, 0.5
q-axis outer loop controller $K_{P5,i}$, $K_{I5,i}$	1, 0.5
q-axis inner loop controller $K_{P6,i}$, $K_{I6,i}$	5×10^{-2}, 0.5

TABLE AII

PARAMETERS OF THE AC COLLECTION GRID AND HVDC TRANSMISSION SYSTEM

AC collection grid	
Transformer ratio k_1	30
Transformer equivalent resistance R_{T1} (mΩ)	7.9
Transformer equivalent inductance L_{T1} (mH)	0.8
Nominal collection grid voltage $u_{PCC,n}$ (kV)	35
Collection grid equivalent resistance $R_{cg,i}$ (mΩ)	305.4
Collection grid equivalent inductance $L_{cg,i}$ (mH)	5.5
HVDC transmission system	
Transformer ratio k_2	6.3
Transformer equivalent resistance R_{T2} (mΩ)	55.4
Transformer equivalent inductance L_{T2} (mH)	5.9
Filter capacitor C_h (μF)	71
Nominal HVDC voltage $V_{HVDC,n}$ (kV)	100
Transmission cables equivalent resistance R_{HVDC} (Ω)	6.3
Transmission cables equivalent inductance L_{HVDC} (mH)	147
Filter inductor $L_{HVDC,on}$ (mH)	9.4
onshore HVDC station controller	
d-axis inner loop controller $K_{P7,i}$, $K_{I7,i}$	5×10^{-2}, 0.5
q-axis outer loop controller $K_{P8,i}$, $K_{I8,i}$	0.1, 0.4
q-axis inner loop controller $K_{P9,i}$, $K_{I9,i}$	4, 1

REFERENCES

[1] Y. Xiong, W. Yao, Y. Yao, J. Fang, X. Ai, J. Wen, and S. Cheng, "Distributed cooperative control of offshore wind farms integrated via mtdc system for fast frequency support," *IEEE Trans. Ind. Electron.*, vol. 70, no. 5, pp. 4693–4704, May 2023.

[2] M. M. Kabsha and Z. H. Rather, "Adaptive control strategy for frequency support from mtdc connected offshore wind power plants," *IEEE Trans. Power Electron.*, vol. 38, no. 3, pp. 3981–3991, Mar. 2023.

[3] B. Shao, S. Zhao, B. Gao, Y. Yang, and F. Blaabjerg, "Adequacy of the single-generator equivalent model for stability analysis in wind farms with vsc-hvdc systems," *IEEE Trans. Energy Convers.*, vol. 36, no. 2, pp. 907–918, Jun. 2021.

[4] Y. Cheng, L. Fan, J. Rose, S.-H. Huang, J. Schmall, X. Wang, X. Xie, J. Shair, J. R. Ramamurthy, N. Modi *et al.*, "Real-world subsynchronous oscillation events in power grids with high penetrations of inverter-based resources," *IEEE Trans. Power Syst.*, vol. 38, no. 1, pp. 316–330, Jan. 2023.

[5] L. Wang, X. Xie, Q. Jiang, H. Liu, Y. Li, and H. Liu, "Investigation of ssr in practical dfig-based wind farms connected to a series-compensated power system," *IEEE Trans. Power Syst.*, vol. 30, no. 5, pp. 2772–2779, Sept. 2015.

[6] A. E. Leon, "Integration of dfig-based wind farms into series-compensated transmission systems," *IEEE Trans. Sustain. Energy*, vol. 7, no. 2, pp. 451–460, Apr. 2016.

[7] H. Liu, X. Xie, J. He, T. Xu, Z. Yu, C. Wang, and C. Zhang, "Subsynchronous interaction between direct-drive pmsg based wind farms and weak ac networks," *IEEE Trans. Power Syst.*, vol. 32, no. 6, pp. 4708–4720, Nov. 2017.

[8] B. Huang, H. Sun, Y. Liu, L. Wang, and Y. Chen, "Study on subsynchronous oscillation in d-pmsgs-based wind farm integrated to power system," *IET Renew. Power Gener.*, vol. 13, no. 1, pp. 16–26, 2019.

[9] G. Li, Y. Chen, A. Luo, Z. He, H. Wang, Z. Zhu, W. Wu, and L. Zhou, "Analysis and mitigation of subsynchronous resonance in series-compensated grid-connected system controlled by a virtual synchronous generator," *IEEE Trans. Power Electron.*, vol. 35, no. 10, pp. 11 096–11 107, Oct. 2020.

[10] B. Shao, S. Zhao, Y. Yang, B. Gao, and F. Blaabjerg, "Subsynchronous oscillation characteristics and analysis of direct-drive wind farms with vsc-hvdc systems," *IEEE Trans. Sustain. Energy*, vol. 12, no. 2, pp. 1127–1140, Apr. 2021.

[11] T. Xue, J. Lyu, H. Wang, and X. Cai, "A complete impedance model of a pmsg-based wind energy conversion system and its effect on the stability analysis of mmc-hvdc connected offshore wind farms," *IEEE Trans. Energy Convers.*, vol. 36, no. 4, pp. 3449–3461, Dec. 2021.

[12] Z. Zhang, P. Kou, Y. Zhang, and D. Liang, "Coordinated predictive control of offshore dc collection grid and wind turbines for frequency response: A scheme without secondary frequency drop," *IEEE Trans. Sustain. Energy*, 2023.

[13] P. T. Nguyen, S. Stüdli, J. H. Braslavsky, and R. H. Middleton, "Lyapunov stability of grid-connected wind turbines with permanent magnet synchronous generator," *Eur. J. Control*, vol. 65, p. 100615, 2022.

[14] L. He and C.-C. Liu, "Parameter identification with pmus for instability detection in power systems with hvdc integrated offshore wind energy," *IEEE Transactions on Power Systems*, vol. 29, no. 2, pp. 775–784, Mar. 2014.

[15] P. S. Kundur and O. P. Malik, *Power system stability and control*. McGraw-Hill Education, 2022.